Enhanced higher harmonic generation from nodal topology

Ching Hua Lee[2,*] Han Hoe Yap,[2,3] Tommy Tai[4] Gang Xu,[5] Xiao Zhang,[1,†] and Jiangbin Gong[2,‡]

[1]*School of Physics, Sun Yat-sen University, Guangzhou 510275, China*

[2]*Department of Physics, National University of Singapore, Singapore, 117542*

[3]*NUS Graduate School for Integrative Sciences and Engineering, Singapore 117456, Republic of Singapore*

[4]*Cavendish Laboratory, University of Cambridge, JJ Thomson Avenue, Cambridge CB3 0HE, Cambridge, United Kingdom*

[5]*Wuhan National High Magnetic Field Center and School of Physics, Huazhong University of Science and Technology, Wuhan 430074, China*

(Received 16 September 2019; accepted 6 July 2020; published 21 July 2020)

Among topological materials, nodal loop semimetals are arguably the most topologically sophisticated, with their valence and conduction bands intersecting along arbitrarily intertwined nodes. But unlike the well-known topological band insulators with quantized edge conductivities, nodal loop materials possess topologically nontrivial Fermi surfaces, not bands. Hence an important question arises: Are there also directly measurable or even technologically useful physical properties characterizing nontrivial nodal loop topology? In this paper, we provide an affirmative answer by showing that nodal linkages *protect* the higher harmonic generation (HHG) of electromagnetic signals. Specifically, nodal linkages enforce nonmonotonicity in the intraband semiclassical response of nodal materials, which will be robust against perturbations preserving the nodal topology. These nonlinearities distort incident radiation and produce higher frequency peaks in the teraHertz (THz) regime, as we quantitatively demonstrate for a few known nodal materials. Since THz sources are not yet ubiquitous, our new mechanism for HHG will greatly aid applications like material characterization and nonionizing imaging of object interiors.

DOI: 10.1103/PhysRevB.102.035138

About a decade ago, topological materials were born when signatures of quantum spin Hall states were detected in HgTe quantum wells [1]. Since then, intensive search has returned various alternative topological material candidates [2,3] with promise in applications like dissipationless wire interconnects [4–7]. More recently, the scope of topological materials has expanded to also include gapless 3D nodal systems like Weyl and nodal line semimetals, where the *Fermi surface* itself is topologically nontrivial [8–12]. In particular, nodal lines have been experimentally observed in $PbTaSe_2$ [13], BiTeI [14], ZrSiTe, ZrSiSe [15], the centrosymmetric superconductor $SnTaS_2$ [16], and, in the form of nodal chains, TiB_2 [17].

Compared to conventional topological insulators which fall into $\mathbb{Z}_2$ or $\mathbb{Z}$ topological classes [18,19], nodal loop semimetals (NLSMs) possess far richer topology, with their nodal loops knotted or linked in unlimited topologically distinct ways [20–22]. A NLSM consists of valence and conduction bands intersecting along so-called nodal lines in 3D momentum space. When these band intersections occur at approximately constant energy, a small chemical potential will result in Fermi regions in the shape thin "tubes" along the nodal lines, even if a small gap prevents perfect band degeneracy. Depending on the crystal symmetry, these Fermi tubes can close to form nodal loops (NLs) that touch to form nodal chains, or link/entangle among themselves to form nodal links/knots (Fig. 4), as proposed in *ABC*-stacked graphdiyne [12] and Co_2MnGa [23]. Even with only one NL, the possible topologies are already uncountably infinite: The loop can cross itself from above or below any number of times, with each permutation leading to a multitude of other knotted configurations. With three or more loops, the nodal structure can even be nontrivially linked despite having no pairwise linkage, as in a Borromean-ring configuration characterized by the Milnor topological invariant [24–26]. Such is the richness of nodal topologies that no single topological invariant can unambiguously distinguish between all topologically distinct configurations.

While quantized Hall conductivity is the hallmark of nontrivial band topology in topological insulators, it is so far unclear what distinct experimental signature corresponds to nontrivial NL topology [27]. The existence of a NL and its surface states is known to give rise to weak antilocalization [28] and spin-resolved transport [29] signatures, respectively, but these properties cannot resolve the topology of nodal linkages. Progress has been made through Berry phase interference measurements around nodal structures, which yield homotopy data that can be used to map out the nodal topology [30,31]. However, such experiments involve intricately specified paths whose very design require *a priori* knowledge of the nodal structure. Furthermore, they are impractical except in nodal cold-atom systems, for which probing techniques like Bloch state tomography and center-of-mass response measurements are applicable and mature [30]. For characterizing actual NLSM materials, the only experimental recourse so far had been ARPES measurements [13,23], although they are arguably indirect approaches involving extensive data reconstruction. Only with a more definitive experimental signature

*phylch@nus.edu.sg
†zhangxiao@mail.sysu.edu.cn
‡phygj@nus.edu.sg

can the mathematical appeal of nodal topology be elevated to phenomenological significance.

In this paper, we show that this sought-after topological signature can be found in the enhancement of higher harmonic generation (HHG) in NLSMs. Although HHG is a generic feature of nonlinear response and has been reported in various 3D materials [32–34] including nodal materials like Cd_3As_2 and TaAs [35–37], it has not been discussed how this HHG can be enhanced by nontrivial nodal topology. Specifically, we demonstrate that NL linkages impose lower bounds on the nonlinearity of their intraband optical response, hence ensuring robust HHG as long as the nodal topology remains undisturbed. While nodal points and lines are already known to exhibit interesting HHG and magneto-optical responses due to their peculiar density of states [38,39], no existing works have shown how these properties can possibly be protected or at least enhanced by topology. Indeed, existing studies have typically been perturbative, unable to access the nonperturbative regime where the incident field impulse is large enough to probe the nodal linkage. Through a semiclassical Boltzmann approach, we shall explore the effects of arbitrarily strong fields and demonstrate generic significant enhancement of HHG by nodal topology. For a few experimentally relevant (slightly gapped) NLSMs, namely, Ti_3Al, YH_3, and Co_2MnGa, we shall also provide quantitative estimates of this enhancement contribution in the THz regime, which is sought after in technological applications like nonionizing imaging and materials characterization [40,41].

I. NONLINEAR SEMICLASSICAL RESPONSE

We first describe the semiclassical Boltzmann approach, from which the response curves of a 3D electronic material can be determined from the shape of its Fermi region. Similar semiclassical approaches have been highly successful in explaining phenomena such as Hall effects and quantum oscillations in diverse settings [42], as well as Bloch oscillations and Berry curvature effects in the context of HHG [43–45]. Subject to an external $\mathbf{E}$ field, the response current is given by [46]

$$\mathbf{J} = \sum_n \int d^3\mathbf{k}\, g(\varepsilon_n(\mathbf{k}))\langle \mathbf{n},\mathbf{k}|\mathbf{J}|\mathbf{n},\mathbf{k}\rangle, \tag{1}$$

where $g(\varepsilon_n(\mathbf{k}))$ is the nonequilibrium occupation function that depends explicitly on the energy dispersion $\varepsilon_n(\mathbf{k})$ of the nth occupied band, and implicitly on $\mathbf{E}$ through g. The semiclassical assumption is that the collective effect of a multitude of possible many-body processes can be simply encapsulated by the behavior of $g(\varepsilon(\mathbf{k}))$ and $\langle \mathbf{k}|\mathbf{J}|\mathbf{k}\rangle$, which holds as long as the electrons are well-described by a Fermi liquid [47]. Under the constant relaxation time approximation (RTA), the electronic occupation function g satisfies the Boltzmann's equation,

$$\frac{dg}{dt} = \frac{\partial g}{\partial t} + \dot{\mathbf{k}}\cdot\frac{\partial g}{\partial \mathbf{k}} = \frac{f-g}{\tau}, \tag{2}$$

such that it "relaxes" to the local equilibrium (Fermi-Dirac) distribution $f = F(\varepsilon(\mathbf{k})) = (1+e^{\beta\varepsilon(\mathbf{k})})^{-1}$ at a rate inversely proportional to the relaxation time τ, which can be computed from a microscopic model for the scattering processes [48]. Physically, $\frac{d}{dt} = \frac{\partial}{\partial t} + \dot{\mathbf{k}}\cdot\frac{\partial}{\partial \mathbf{k}}$ is the phase-space convective derivative, which when acted on g gives the correction $(f-g)/\tau$ to the continuity equation due to scattering. We have omitted spatial dependencies $\frac{\partial g}{\partial \mathbf{r}}$ since we are not considering thermal or chemical gradients.

The effect of an external field $\mathbf{E}$ enters the semiclassical equations of motion (EOMs) for electronic wave packets, which take a manifestly symmetric form when expressed in units where electronic mass, charge, and $\hbar$ are all set to unity:

$$\dot{\mathbf{r}} = \mathbf{v} + \dot{\mathbf{k}}\times\mathbf{\Omega}, \tag{3a}$$

$$\dot{\mathbf{k}} = \mathbf{E} + \dot{\mathbf{r}}\times\mathbf{B}. \tag{3b}$$

Here, $(\mathbf{r},\mathbf{k})$ are the center-of-mass phase space coordinates of an electron wave packet. In this work, we shall not consider the effects of a magnetic field, and set $\mathbf{B}=\mathbf{0}$. The wave-packet group velocity $\mathbf{v} = \nabla_{\boldsymbol{k}}\varepsilon(\mathbf{k})$ and Berry curvature $\mathbf{\Omega} = \mathbf{\Omega}(\mathbf{k})$ it feels are both explicit functions of the wave-packet momentum $\mathbf{k}$. Due to translation invariance implied by Eq. (2), g is only affected by the Lorentz force $\dot{\mathbf{k}}$, and not $\dot{\mathbf{r}}$.

To derive the explicit response dependence on the nodal structure, we shall focus on the ballistic regime where τ dominates all other timescales, such that closed form solutions exist for g and hence the response current $\mathbf{J}$. In particular, this requires that $\Omega\tau \gg 1$, where $\mathbf{E}(t) \sim \mathbf{E}(0)e^{i\Omega t}$, a reasonable constraint in the THz regime ($\Omega \sim 20-100$ THz) where $\Omega\tau$ can be estimated to lie between 10 to 50 for known nodal materials [45]. In this ballistic regime, scattering processes cannot catch up with the much shorter oscillation timescales [44,49], and we do not expect g to be close to the local equilibrium f at all; instead, g obeys the very intuitively attractive solution

$$g(\mathbf{k},t) = F\left(\varepsilon\left(\mathbf{k} - \int_{-\infty}^{t}\mathbf{E}(t')dt'\right)\right) = F(\varepsilon(\mathbf{k}-\mathbf{A}(t))), \tag{4}$$

which can be easily verified viz. Eq. 3(b), which gives $\frac{dg}{dt} = \frac{dF}{d\varepsilon}\mathbf{v}\cdot(\dot{\mathbf{k}}-\mathbf{E}(t)) = 0$. Equation (4) elegantly expresses the nonequilibrium electronic distribution function g as the usual Fermi-Dirac distribution with momentum shifted (minimally coupled) by an arbitrarily large impulse [50]: $\mathbf{k}\to\mathbf{k}-\mathbf{A}(t)$, where $\mathbf{A}(t) = \int_{-\infty}^{t}\mathbf{E}(t')dt'$. With this, and assuming that only one occupied band exists from now on, the current is simply given by

$$\begin{aligned}\mathbf{J}[\mathbf{A}(t)] &= \int d^3\mathbf{k}\, g(\mathbf{k},t)\,\dot{\mathbf{r}}\\ &= \int d^3\mathbf{k}\, F(\varepsilon(\mathbf{k}-\mathbf{A}(t)))[\mathbf{v}-\mathbf{\Omega}\times\mathbf{E}(t)]\\ &= n[e\langle\mathbf{v}\rangle_{\mathbf{E}} + \mathbf{E}(t)\times\langle\mathbf{\Omega}\rangle_{\mathbf{E}}],\end{aligned} \tag{5}$$

where $n = \int g(\mathbf{k},t)d^3\mathbf{k}$ is the electronic density and $\langle\mathbf{v}\rangle_{\mathbf{E}} = \int g(\mathbf{k},t)\,\mathbf{v}\,d^3\mathbf{k}/n$, $\langle\mathbf{\Omega}\rangle_{\mathbf{E}} = \int g(\mathbf{k},t)\,\mathbf{\Omega}\,d^3\mathbf{k}/n$ are the integrated electron velocity and Berry curvature over the Fermi region, i.e., region in the Brillouin zone (BZ) where $g(\mathbf{k},t)$ is nonzero (The factor of $\frac{e^2}{\hbar}$ in front of the second term has been set to one in our choice of units.). For small chemical potentials such that the occupied states remain close to the NLs, the Fermi region takes the shape of the nodal tubes, but is shifted by an electromagnetic impulse $\int^t \mathbf{E}(t')dt'$ [Eq. (4)].

Equation (5) is the main result from our semiclassical approach and forms the starting point of our analysis [51].

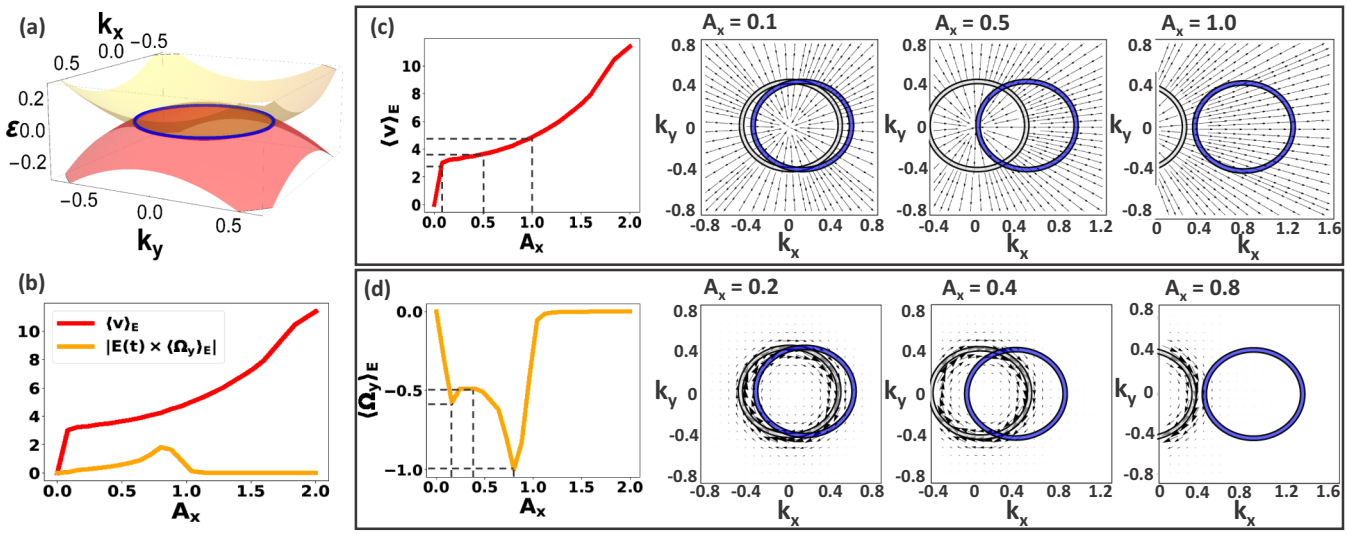

FIG. 1. Unprotected nonlinear response of a topologically trivial single NL. (a) Illustrative energy dispersion in the $k_z = 0$ slice defined by Eq. (6) with $\mu = 0.03$, $r = 2.6$, and $T = 10$K. (b) Resultant current response from both contributions, which is monotonic despite being nonlinear. The Berry curvature contribution is typically subdominant for illustrative parameters drawn from realistic nodal ring materials. (c) Elaboration of the $\langle v_x \rangle_{\mathbf{E}}$ contribution, in arbitrary units, to the longitudinal response from interferences in velocity vector field. The partial cancellation of $\mathbf{v} = \nabla_{\boldsymbol{k}} \varepsilon(\mathbf{k})$ at electromagnetic vector potential $A_x \sim E_x/\Omega$ comparable to the NL radius (center) suppresses the increase of $J_x(A_x)$, but not sufficiently strong to create a response kink (red curve). (d) Transverse $\langle \Omega_y \rangle_{\mathbf{E}}$ contribution to the response from interferences in Berry flux field, shown for $r = 2.9$. Since the Berry curvature is strongly concentrated around the NL, the response peaks only when the Fermi tube overlaps considerably with the NL. The smaller peak at $A_x \approx 0.1$ is, however, partially suppressed by opposite contributions from both sides of the NL.

It expresses the response current in terms of $\langle \mathbf{v} \rangle_{\mathbf{E}}$ and $\langle \boldsymbol{\Omega} \rangle_{\mathbf{E}}$, which themselves depend on $\mathbf{E}$ in a manner prescribed by the shape of the Fermi region. Note that both $\langle \mathbf{v} \rangle_{\mathbf{E}}$ and $\langle \boldsymbol{\Omega} \rangle_{\mathbf{E}}$ can both contain longitudinal and Hall components, and depend strongly on the relative signs of $\mathbf{v}$ and $\boldsymbol{\Omega}$ contributions within the nodal tube. Although we have derived Eq. (5) for only the intraband contributions in the ballistic regime, our following main results, which are ultimately concerned with topological properties, should still remain valid in the presence of weak scattering.

II. NONLINEAR RESPONSE ENHANCED BY NONTRIVIAL NODAL TOPOLOGY

To illustrate how topological nodal linkages enforce nonlinearity in the current response, we first review the origin of unprotected nonlinear response in a single NL without any linkage, and next demonstrate how this nonlinearity can be protected when a nodal linkage (Hopf link) is introduced.

A. Single nodal loop without topological linkage

As with other nodal systems like graphene and Weyl semimetals [38,52,53], a single NL exhibits unconventional [54] (though nontopological) nonlinear response behavior. With its non-topological origins, the actual extent of nonlinearity differs greatly among NLs with different dispersion and occupancy details. Consider a minimal NL Hamiltonian,

$$H_{\mathrm{NL}}(\mathbf{k}) = \big(\cos k_x + \cos k_y + \cos k_z - r\big)\sigma_x + \sin k_z \sigma_y + M\sigma_z, \tag{6}$$

where σ_x, σ_y are the Pauli matrices, $1 < r < 3$ and M is an extremely small gap introduced so the Berry curvature is well-defined. To emphasize the generality of our follow arguments, we shall not fix the physical parameters till we discuss the material candidates later. That $H_{\mathrm{NL}}(\mathbf{k})$ describes a NL can be seen from its energy dispersion,

$$\varepsilon_{\mathrm{NL}}(\mathbf{k}) = \pm\sqrt{M^2 + \sin^2 k_z + \big(\cos k_x + \cos k_y + \cos k_z - r\big)^2}, \tag{7}$$

which is minimally gapped along the $\cos k_x + \cos k_y = r - 1$ loop in the $k_z = 0$ plane. At small chemical potential $\mu > M$ and temperature β^{-1}, the occupied states are approximately contained in a tube of radius $\mu - M$ around this NL [Fig. 1(a)].

In the presence of an oscillatory electric field $\mathbf{E}(t) = E(t)\hat{x}$, Eq. (4) dictates that the Fermi tube of occupied states is translated in the field direction according to the momentum shift $\mathbf{k} \to \mathbf{k} - \mathbf{A}(t)$. Due to this shift, the expectation values $\langle \mathbf{v} \rangle_{\mathbf{E}}$ and $\langle \boldsymbol{\Omega} \rangle_{\mathbf{E}}$ over the Fermi tube differs from their equilibrium values at $\mathbf{E} = \mathbf{0}$, where $\langle \mathbf{v} \rangle_{\mathbf{E}=\mathbf{0}}$ always vanishes.

As given by Eq. (5), the nonlinear current response arises from both the $\langle \mathbf{v} \rangle_{\mathbf{E}}$ and $\mathbf{E} \times \langle \boldsymbol{\Omega} \rangle_{\mathbf{E}}$ contributions. Manifestly from Fig. 1(c), the velocity field $\mathbf{v} = \nabla_{\boldsymbol{p}} \varepsilon(\mathbf{p})$ points radially outward outside the NL, and radially inward inside the NL, i.e., is always pointing toward higher energies. The Berry curvature $\langle \boldsymbol{\Omega} \rangle_{\mathbf{E}}$, on the other hand, circulates clockwise, and is concentrated along the circumference of the NL as given by

$$\boldsymbol{\Omega}_{\mathrm{NL}}(\mathbf{k}) = \frac{M \cos k_z}{2|\varepsilon_{\mathrm{NL}}(\mathbf{k})|^3} \begin{bmatrix} \sin k_y \\ -\sin k_x \\ 0 \end{bmatrix}. \tag{8}$$

As the applied field increases, the response behavior transits between a few distinct regimes, as illustrated in Figs. 1(c) and 1(d). In the linear regime of small $\mathbf{A}$ shifts, both

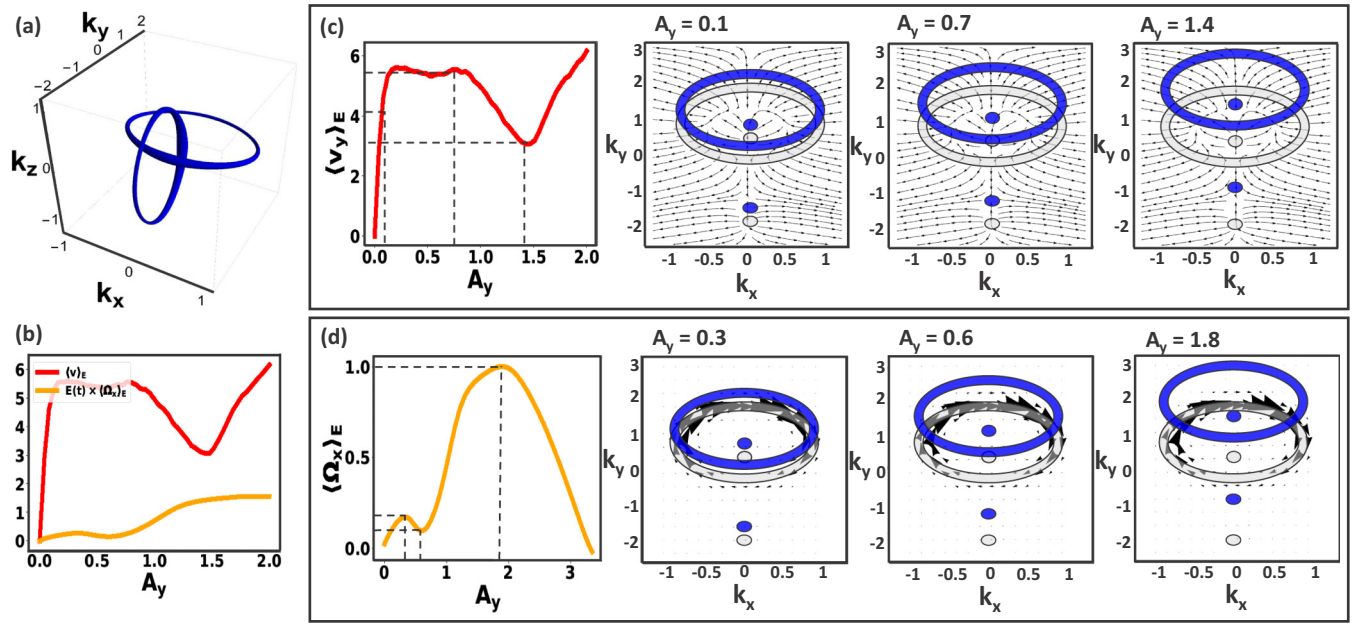

FIG. 2. Response nonlinearity enhanced and protected by topological linkage. (a) Nodal structure of an illustrative Hopf linkage between two NLs oriented perpendicular to $\hat{e}_x$ and $\hat{e}_z$, as defined by Eq. (9) with $\mu = 0.1$, $r = 2.6$, and $T = 10$ K. (b) Resultant current, which is highly nonlinear due to the topological linkage. (c) Elaboration of the $\langle v_y \rangle_{\mathbf{E}}$ contribution to the longitudinal response, which exhibits much stronger nonlinearity (with large kink) than that of the single NL of Fig. 1. The cancellation of its $\mathbf{v} = \nabla_{\boldsymbol{k}} \varepsilon(\mathbf{k})$ at intermediate values of A_x (center) is reinforced by the singularity in $\mathbf{v}$ created by the other linked NL (small blue circular cross section). (d) $\langle \Omega_x \rangle_{\mathbf{E}}$ contribution to the transverse response, which is greatly enhanced when the other linked NL passes through the region of concentrated Berry flux without experiencing destructive interference.

$\langle \mathbf{v} \rangle_{\mathbf{E}}$ and $\langle \boldsymbol{\Omega} \rangle_{\mathbf{E}}$ pick up slight imbalances from their respective $\mathbf{v}$ and $\boldsymbol{\Omega}$ contributions, and thus rapidly increase. In particular, $\langle \boldsymbol{\Omega} \rangle_{\mathbf{E}}$ peaks when the clockwise/anticlockwise vectors from $\boldsymbol{\Omega}$ dominate. Generically, the response has to be nonlinear due to the "destructive interference" of current contributions: When $\mathbf{A}$ is comparable to the NL radius, the Fermi tube straddles the interior and exterior of the NL and receives simultaneously opposing contributions to both $\mathbf{v}$ and $\boldsymbol{\Omega}$. Due to the more sharply concentrated Berry flux, the $\langle \boldsymbol{\Omega} \rangle_{\mathbf{E}}$ contribution contains more pronounced nonlinearities. Yet, for parameters typical of nodal materials as described later, the $\langle \mathbf{v} \rangle_{\mathbf{E}}$ contribution dominates, resulting in a fairly nonlinear overall current response [Fig. 1(b)].

It has to be emphasized, however, that the above-mentioned response nonlinearity is not necessarily robust. In particular, destructive interference in the dominant $\langle \mathbf{v} \rangle_{\mathbf{E}}$ contribution is subject to details of the curvature in the dispersion, which should not be dependent on the nodal structure. In fact, very different response curves can result from different realizations of the same NL, as shown in the Appendixes [45]. As evident in Fig. 1, the response is indeed still monotonic without a proper kink due to the "roundness" of the dispersion at the center of the NL.

B. Nodal loops with topological linkage

To ensure pronounced nonlinearity in the current response $\mathbf{J}[\mathbf{A}(t)]$, significant destructive interference of $\langle \mathbf{v} \rangle_{\mathbf{E}}$ must be guaranteed at certain values of the applied field $\mathbf{A}$. We shall see that this is assured if the NL is linked by another NL, such that an unremovable singularity passes through it. Consider a simplest nodal Hopf link Hamiltonian [55] possessing two interlinked NLs (Fig. 2),

$$H_{\text{Hopf}}(\mathbf{k}) = \text{Re}[f(v,w)]\sigma_x + \text{Im}\,[f(v,w)]\sigma_y + M\sigma_z, \quad (9)$$

where M is a small gap and $f(v,w) = (v-w)(v+w)$ with $v = \sin(k_z - k_x) + i(2\cos k_x \cos k_z + \cos k_y - r)$ and $w = \sin(k_x + k_z) + i \sin k_y$. $1 < r < 3$ controls the shape and size of each loop as in the NL model, as well as their relative separation. As shown in Fig. 2(a), it consists of two linked NLs normal to $\hat{x}$ and $\hat{z}$, with dispersion explicitly given by

$$\varepsilon_{\text{Hopf}}(\mathbf{k}) = \pm\sqrt{M^2 + \chi^2 + 4(e_1 e_2 - e_3 e_4)^2}, \quad (10)$$

where substitutions $\chi \equiv e_1^2 - e_2^2 - e_3^2 + e_4^2$, $e_1 \equiv \sin(k_z - k_x)$, $e_2 \equiv (\cos(k_x + k_z) + \cos k_y + \cos(k_z - k_x) - r)$, $e_3 \equiv \sin(k_x + k_z)$, and $e_4 \equiv \sin k_y$ have been defined for notational brevity. As plotted in Fig. 2(b), it gives rise to a $\mathbf{v} = \nabla_{\boldsymbol{k}} \varepsilon(\mathbf{k})$ field with sources or sinks within the NLs. These singularities are the cross sections of the other topologically linked NLs, which is analytically given by simultaneous solutions to $e_1^2 + e_4^2 = e_2^2 + e_3^2$ and $e_1 e_2 = e_3 e_4$.

We next show that singularities of the $\mathbf{v}$ vector field can indeed ensure significant nonlinearity in the current response $\mathbf{J}(\mathbf{A})$ by studying the differential response of a thin NL (derived in the Appendixes):

$$\frac{dJ_i}{dA_j} \approx 2 \sum_{\alpha \in \text{NLs}} \frac{\mu}{\hat{e}_j \cdot \mathbf{v}_F} \frac{d^2 \varepsilon(\mathbf{k}^\alpha + \mathbf{A})}{dk_i dk_j}. \quad (11)$$

In the above, $\mathbf{k}^\alpha$ labels the trajectories of all the NLs in the BZ, and $\hat{e}_j \cdot \mathbf{v}_F$ is the component of the Fermi velocity of the αth NL at momentum $\mathbf{k}^\alpha$ along the applied field. In particular, the

longitudinal differential response is proportional to the sum of the curvature of the dispersion along the **A**-displaced NLs. When the curvatures conspire to form a highly fluctuating sum, the current response contains large fluctuating gradients, and becomes significantly nonlinear.

For concreteness, we analyze Eq. (11) with the simplest possible in-plane dispersion hosting a nodal linkage: $\varepsilon^0_{\rm link}(k_x, k_y) = |\sqrt{k_x^2 + k_y^2} - r|$, which describes a circular NL of energy $\varepsilon = 0$ and radius r in the k_x-k_y plane, which is perpendicularly linked by another NL of energy $\varepsilon = r$ at $\mathbf{k} = \mathbf{0}$. To regularize the infinite dispersion curvature at its nodes, we introduce small gaps [56] m_0, m_r at the perpendicular and in-plane rings at $|\mathbf{k}| = 0$ and r, such that the dispersion is modified to

$$\varepsilon_{\rm link}(k_x, k_y) = \sqrt{m_r^2 + \left(\sqrt{k_x^2 + k_y^2 + m_0^2} - \sqrt{r^2 + m_0^2}\right)^2}. \quad (12)$$

Its second derivative $\frac{d^2\varepsilon_{\rm link}}{d^2k_j}$, $j = x, y$, almost vanishes except at the nodes, where it diverges like $\sim -m_0^{-1}$ at the nodal linkage through the origin, and like $\sim m_r^{-1}k_j^2 r^{-2}$ on the $k_x^2 + k_y^2 = r^2$ nodal ring. These divergences are exactly the large curvature fluctuations necessary for a greatly fluctuating differential longitudinal response $\frac{dJ_j}{dA_j}$ [Eq. (11)]. When a (regularized) nodal linkage is present, small gaps m_0, m_r and thus large curvature fluctuations leading to response nonlinearity are inevitable.

We next analyze the response kinks corresponding to these curvature fluctuations. At very small $\mathbf{A}_j$ where the Fermi tube is almost aligned with the NL, $\frac{d^2\varepsilon_{\rm link}(\mathbf{k}^\alpha + \mathbf{A}_j)}{d^2k_j}$ picks up large positive contributions $\sim m_r^{-1}k_j^2 r^{-2}$, giving rise to a large differential response. But at $\mathbf{A}_j \approx r$, $\frac{d^2\varepsilon_{\rm link}(\mathbf{k}^\alpha + \mathbf{A}_j)}{d^2k_j}$ picks up a large negative contribution m_0^{-1} as it cuts the origin, and hence produces a negative differential response. In fact, the differential response of this model has to exhibit a *reversal* due to the opposite signs of dominant curvature contributions, thereby leading to a very *nonmonotonic* and hence highly nonlinear current response containing kink/s, as shown in Fig. 2(c). A qualitatively similar cancellation of oppositely signed contributions also occurs for the Berry curvature [Fig. 2(d)]. In generic topologically linked NL systems, the linkages still enforce similar oppositely signed dispersion curvature contributions, and it is in this sense that their $\langle \mathbf{v} \rangle_{\mathbf{E}}$ response nonlinearity is protected. Strong nonlinearities also analogously dominate the $\langle \mathbf{\Omega} \rangle_{\mathbf{E}}$ contribution to the response, but they typically play a subdominant role.

III. HIGHER HARMONIC GENERATION FROM NONLINEAR RESPONSE

Consider a sinusoidal time-varying applied electric field signal $\mathbf{E}(t) = \mathbf{E}_0 \cos \Omega t$, which corresponds to the vector potential $\mathbf{A}(t) = \mathbf{A} \sin \Omega t$, where $\mathbf{A} = \frac{\mathbf{E}_0}{\Omega} = \frac{\mathbf{p}_0 a}{\hbar}$, $\mathbf{p}_0$ the impulse amplitude vector and a the lattice spacing of the nodal material lattice. We have temporarily reintroduced the physical units in preparation for later experimental discussion. The greater the nonlinearity of the current response function $\mathbf{J}(\mathbf{A})$, the larger the extent of HHG. The extent of signal distortion

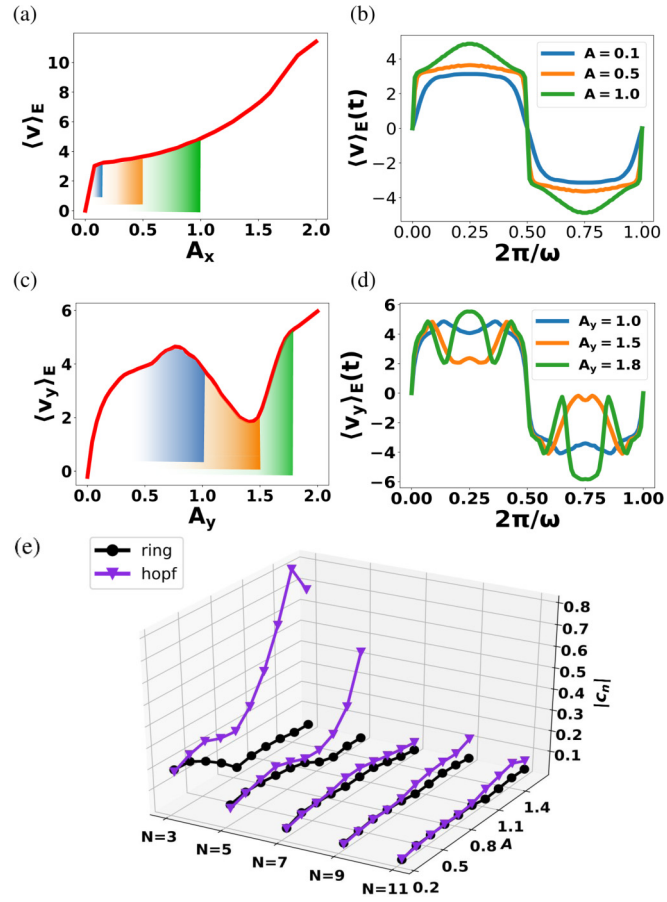

FIG. 3. (a), (c) Response curves of the single NL and Hopf nodal systems of Figs. 1 and 2, respectively, with (b), (d) demonstrating how they distort sinusoidal signals of different amplitudes A (as indicated by corresponding colored regions in the response curves). Due to the nonmonotonic response in the topologically linked Hopf system (c), signal oscillations traversing the kink acquire additional fluctuations of higher frequency (d). The superior HHG by the Hopf system is evident from its larger Fourier coefficient ratios c_n [Eq. (13)] in (e).

between chosen direction components i and j can be quantified via Fourier coefficient ratios c_n describing the higher harmonics:

$$J_j(A_i(t)) = J_j(A \sin \Omega t) \propto \sin \Omega t + \sum_{n \neq 0} c_n \sin n\Omega t. \quad (13)$$

In Figs. 3(c) and 3(d), we see that the pronounced nonmonotonicity of the $\langle \mathbf{v} \rangle_{\mathbf{E}}$ part of the Hopf current response leads to the creation of new higher frequency peaks. While higher harmonics are also present in the the single NL response [Figs. 3(a) and 3(b)], they are manifestly smaller, corresponding only to gentle corrections to sinusoidal current output. As summarized in Fig. 3(e), the Hopf linkage indeed possess much larger c_n for most amplitudes, especially when the amplitude corresponds to the response kink where c_3 and c_5 are close to unity. In more generic NL configurations, i.e., a Borromean ring with topological linkages in multiple planes, the response function in the direction parallel to each plane

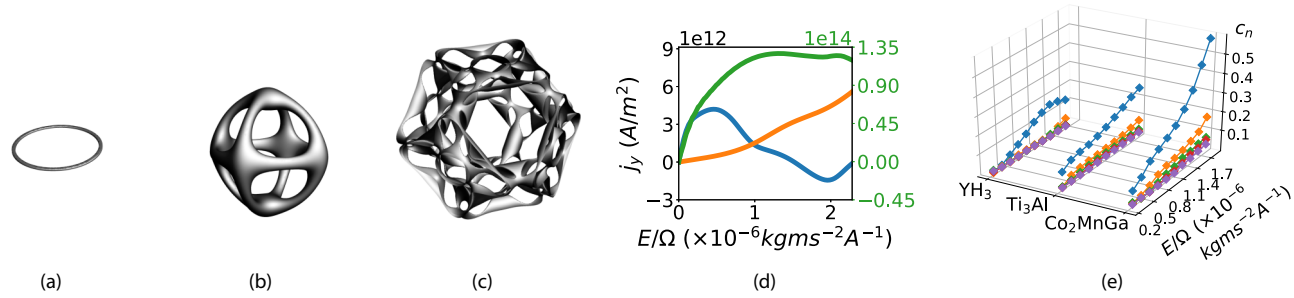

(a) (b) (c) (d) (e)

FIG. 4. Occupied states (Fermi seas) of (a) Ti_3Al, (b) YH_3, and (c) Co_2MnGa. (d) The current response of Ti_3Al (green), YH_3 (orange), and Co_2MnGa (blue) at 10 K with chemical potentials $\mu = 0.15$ eV, 0.002 eV, and 0.130 eV, respectively. The left and right vertical axes denote the numerical current in YH_3/Co_2MnGa and Ti_3Al, arising from electromagnetic impulses E/Ω. (e) The higher harmonic ratios c_n as a function of the driving impulse amplitude p_0, with Co_2MnGa exhibiting by far the strongest HHG due to its multiple nodal linkages. For clarity, the HHG ratios are also individually plotted out in the Appendixes.

will necessarily all exhibit large nonlinearity and hence strong HHG.

IV. HHG IN NODAL MATERIAL CANDIDATES

We now present quantitative calculations of the HHG induced by the nodal topology of three different known nodal materials, arranged in order of increasing topological sophistication. We shall be exclusively concerned with the $\langle \mathbf{v} \rangle_{\mathbf{E}}$ response, since the Berry curvature contribution is typically smaller and depends nonuniversally on the internal structure of the eigenbands.

A. 1. Ti_3Al—single nodal ring

One first nodal material is Ti_3Al, which contains a single almost "ideal" NL whose band crossing is almost dispersionless and very close to the Fermi level [57]. These properties yield a well-defined nodal ring with almost uniform thickness [Fig. 4(a)], qualitatively approximating our toy model from Eq. (7). While its nodal structure has yet to be experimentally verified, high-quality samples of Ti_3Al already exist in both alloy and nanoparticle form [58–60].

To compute its $\langle \mathbf{v} \rangle_{\mathbf{E}}$ current response, we employ its Density Functional Theory (DFT)-fitted energy dispersion from Ref. [57], as described in the Appendixes [45]. Like the single NL toy model, Ti_3Al exhibits some nonlinearity in its current response, although hardly large enough to exhibit nonmonotonicity [green curve in Fig. 4(d)]. Correspondingly, its HHG ability is limited, with even the lowest $n = 3$ harmonic generation ratio c_3 being below 30% [Fig. 4(e)].

B. 2. YH_3—three touching nodal rings

Next up in sophistication is the material YH_3, which is proposed to contain three orthogonal NLs that surround the Γ point [61]. These NLs are protected by nonsymmorphic symmetry present in its $P\bar{3}c1$ form, which is likely to be its most stable crystal structure as seen from neutron-diffraction experiments [62,63].

While its three NLs are isolated from other bands, they intersect instead of linking each other [Fig. 4(b)]. To explore whether the absence of linkages penalize HHG, we first construct its tight-binding model according to a DFT-fitted ansatz detailed in the Appendixes [45]. As evident in Figs. 4(d) and 4(e), the resultant $\langle \mathbf{v} \rangle_{\mathbf{E}}$ response nonlinearity and hence HHG for the three touching NLs of YH_3 is even weaker than that of the single NL Ti_3Al, even before spin-orbit coupling effects gap out NLs into elogated Fermi tubes. The reason for the poor HHG is that, in this case, the multiple NLs "smooth" out the energy dispersion around the nodal touchings, thereby reducing the total potential for destructive interference of velocity velocities.

C. 3. Co_2MnGa—intertwined nodal flower petals, rings, etc.

We now turn to our third and most topologically sophisticated material, the magnetic Heusler compound Co_2MnGa which was theoretically predicted in 2017 [64] and soon realized experimentally by various groups [23,65,66]. In Ref. [23], the intricate nodal structure of Co_2MnGa was revealed to contain Hopf links, inner and outer chains at the Fermi energy, as shown in Figs. 4(c) and 5. While Co_2MnGa contains even more nodal components than YH_3, the crucial difference is that many of its components are *topologically linked* and not just touching each other.

As illustrated in Fig. 6, Co_2MnGa contains six linked NLs (red) which are shaped like flower petals [Fig. 6(a)]. They touch smaller, circular NLs (blue), dubbed outer chains, as shown in Fig. 6(b). These blue loops are, in turn, in contact with four smaller, also circular NLs (green), as in Fig. 6(c), forming another set of outer chains. Finally, the green rings touch the red flower petals, constituting an inner chain [Fig. 6(d)]. All these features of Co_2MnGa contribute to a strongly nonlinear response curve with large HHG coefficients, as presented in Figs. 4(d) and 4(e). These results were computed from a tight-binding model fitted to first-principles calculation results [64].

The characteristically kink response curve of Co_2MnGa gives rise to much larger $n = 3$ and 5 harmonics than from YH_3 and Ti_3Al and can be pedagogically explained via a detailed breakdown of its various topological NL linkages. We shall focus on the six red flower petals and the six blue rings, which are the dominant current contributors [largest features in Fig. 6(j)]. Their individual contributions can be isolated through a two-band approximate model which is amenable to

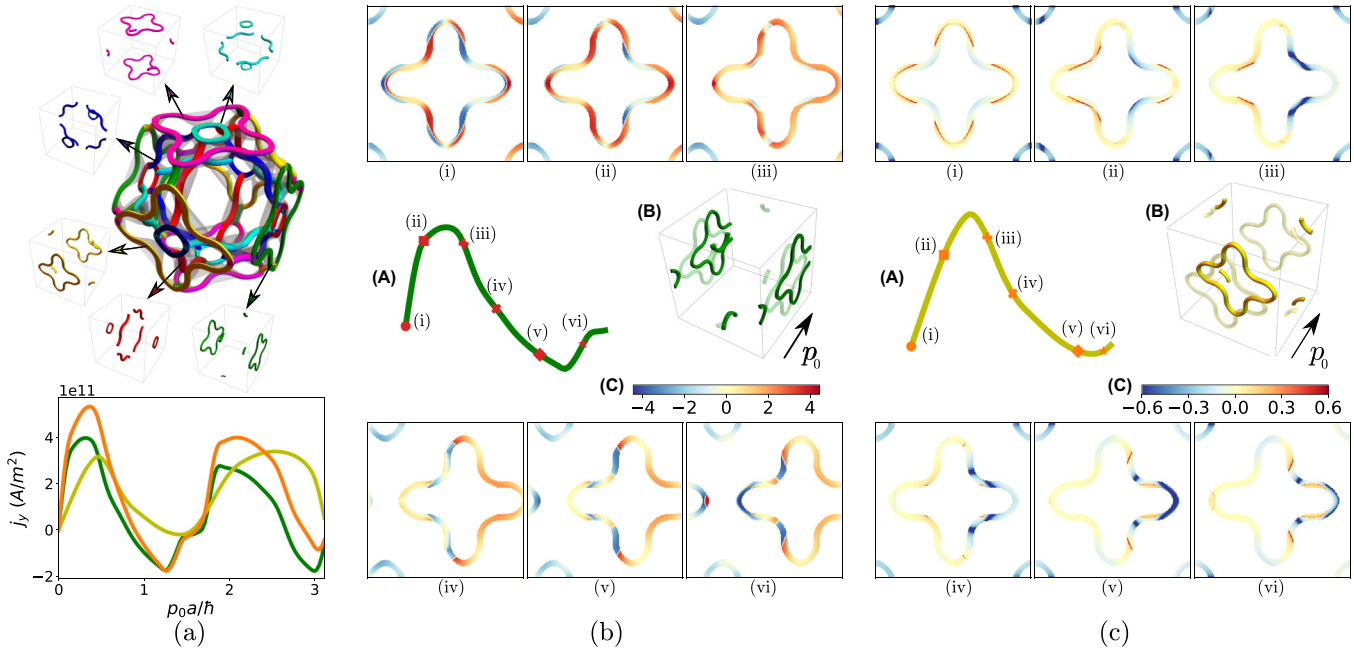

FIG. 5. Decomposition of the current response of Co_2MnGa into those of its constituent nodal features. (a) Top: Breakdown of its nodal structure into dominant nodal Hopf flower petals and rings whose linkages are further detailed in Fig. 6. Bottom: Total current response (orange, scaled down by a factor of four for clarity) from the sum of green/magenta/red/cyan and yellow/blue nodal structure responses, which correspond to only two unique curves due to cubic symmetry.(b), (c) (A) response curves of the green/yellow Hopf flower petals in the directions indicated by the impulse p_0, as illustrated in the insets (B). The response curve shapes at various impulse strengths (i)–(vi) can be understood through integrating the explicit electronic group velocity profiles within the petals, as illustrated in the corresponding upper and lower panels. Legend colorbars (C) for the group velocities are given in units of $\times 10^5$ ms^{-1}.

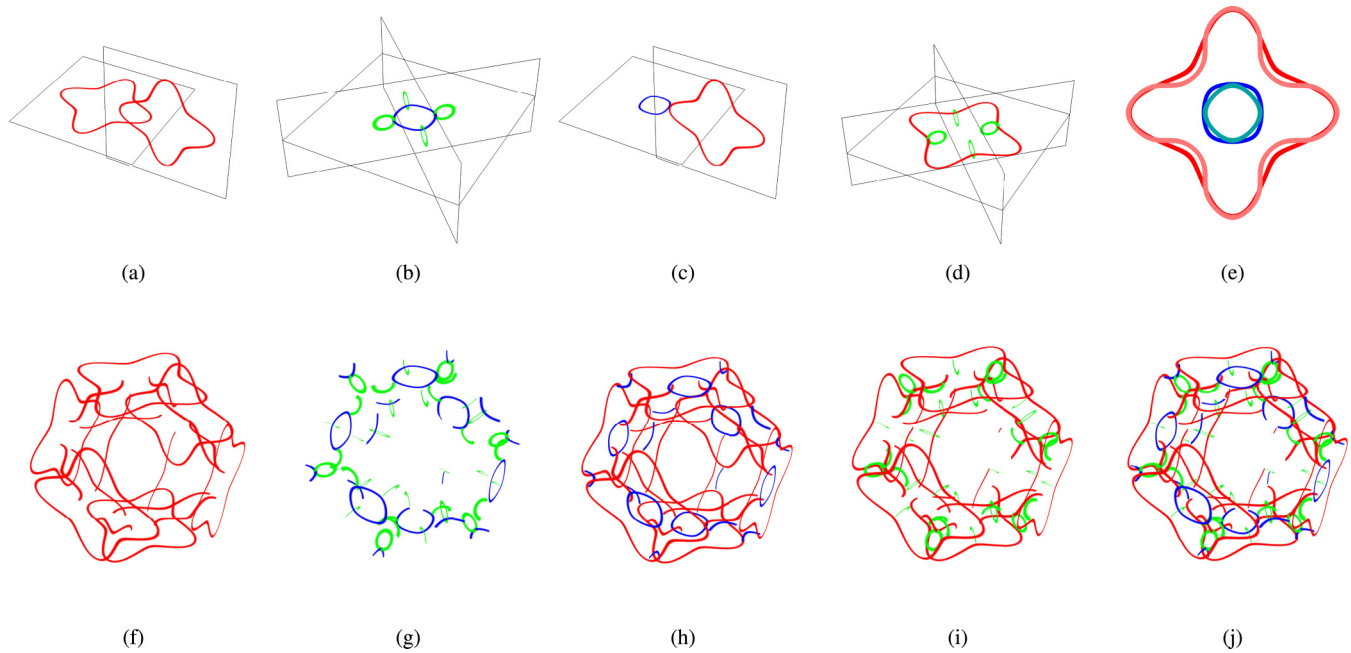

FIG. 6. The assembly of all nodal features of $CoMn_2Ga$ into a linked nodal network. Mostly saliently, it involves Hopf links [Figs. 6(a) and 6(f)], inner chains [Figs. 6(d) and 6(i)] and outer chains [Figs. 6(b), 6(c), 6(g) and 6(g)]. Specifically, it consists of a (a) Hopf link between red flower petals, (b) outer chain involving a blue loop and four smaller green loops, (c) outer chain formed by a blue loop and a flower petal, (d) inner chain due to a flower petal and four green rings. These features form subnetworks of linkages: (f) network of Hopf links, (g) network of outer chains formed from blue and green loops, (h) network of outer chains formed from blue loops and red flower petals, (i) network of inner chains, which together form the full nodal network (j). Within it, the red flower petals and blue loops occupies the greatest volume and hence dominate the response. As shown in (e), their Fermi surfaces are decently approximated by our two-band model (pink flower petal and cyan loop). For graphical completeness, all nodal structures are displayed not in the first Brillouin zone (a truncated octahedron), but on a cube twice its size.

analytic decomposition as follows:

$$H_{\mathrm{Co_2MnGa}} = \mathrm{Re}[f(\mathbf{k})]\sigma_1 + \mathrm{Im}\,[f(\mathbf{k})]\sigma_3, \tag{14}$$

where $f(\mathbf{k}) = \Pi_{n=1}^{6}(u_n + \mathrm{i}v_n)$, which is a product of constituent nodal structures described by

$$\begin{aligned} u_{\mathrm{even}} &= [\cos^3(k_x/2) + \cos^3(k_y/2) + \cos^3(k_z/2) - m], \\ u_{\mathrm{odd}} &= [\cos^3(k_x/2) + \cos^3(k_y/2) + \cos^3(k_z/2) + m], \end{aligned} \tag{15}$$

and $v_{1,2} = \sin(k_x/2)$, $v_{3,4} = \sin(k_y/2)$, $v_{5,6} = \sin(k_z/2)$, the parameter $m = -0.5$ chosen so the Fermi surface approximates that of Co_2MnGa. Remarkably, such a simple construction yields a rather accurate reconstruction of the Fermi surface of Co_2MnGa, as illustrated by its cross section comparison in Fig. 6(e) and the 3D superimposition in Fig. 5(a).

Based on this approximate model, we can extract and compare the response contributions of the individual dominant NLs of $CoMn_2Ga$, which are the six flower petals and rings relabeled cyan, magenta, blue, yellow, red, and green in the top panel of Fig. 5(a). Interestingly, for an applied driving field along one of the rectangular coordinate axes, i.e., $\hat{y}$, all these nodal structures obey only two possible response curves (type I: yellow and blue; type II: magenta, green, red, cyan). This follows from the cubic symmetry of Co_2MnGa and enables a transparent reconstruction of the overall response. The two possible responses are presented in Figs. 5(b) and 5(c), where the green and yellow response curves correspond, respectively, to the contributions of the representative green and yellow nodal structures from Fig. 5(a). Curves from the other structures are equivalent to one of these, and are omitted for brevity. Together, both response curves exhibit large kinks, with their contrasting behavior at larger fields interfering to give rise to even more pronounced nonlinearity and hence HHG properties, as detailed in the Appendixes. Their total contribution, plotted in Fig. 5(a), indeed qualitatively agrees with the full response curve from Fig. 4(d), despite considerable simplifications [67]. Its far larger nonlinearity compared to that of YH_3 attests to the fact that to yield strong HHG, NLs must *topologically link* and not merely intersect each other.

V. DISCUSSION

In this paper, we uncovered a very physically measurable consequence of topological nodal linkages, namely, that they enhance and protect the HHG of optical radiation, which can be useful for terahertz applications. As such, the sophisticated topology of nodal knots and link networks are no longer mere mathematical curiosities, but are in principle reconstructible from nonlinear response data in various directions. By venturing beyond the perturbative regime, we are able to access the effect of field impulses comparable to the size of NLs and unveil the key role of nontrivial nodal linkages in enhancing the HHG already known to exist in simple nodal structures [38,39].

Our results rigorously hold in the ballistic limit, which corresponds to the terahertz regime for scattering times expected of high mobility samples of known nodal materials. Due to the robustness of our HHG mechanism, the characteristically superior HHG from nodal linkages is likely to extend beyond the ballistic and semiclassical limits, at least until hot phonon or interband scattering dominate. Despite our semiclassical analysis, our results crucially rely on the Fermi sea condensation of electrons, which is fundamentally due to the *quantum mechanical* exclusion principle. As such, they are distinct from signatures of nodal geometry proposed in purely classical settings, such as slow light and anomalous refraction in photonic crystals [68–74] or topolectrical resonances due to nodal drumhead states [55,75–77].

Reassuringly, the HHG enhancement by nodal linkages is also in consonance with quantitative response computations of three known representative nodal materials Ti_3Al, YH_3, and Co_2MnGa. In particular, the essential role of nodal linkages cannot be more evident from the comparison between Co_2MnGa and YH_3: Co_2MnGa, which contains multiple nodal linkages, exhibits far stronger HHG than YH_3, which contains multiple nodal intersections.

ACKNOWLEDGMENTS

We thank G. Chang, Y. W. Ho, Y. S. Ang, and J. Song for discussions. J.G. is supported by the Singapore NRF Grant No. NRF-NRFI2017-04 (WBS No. R-144-000-378-281).

APPENDIX A: VALIDITY OF THE BALLISTIC APPROXIMATION

To justify that the ballistic regime $\Omega\tau \gg 1$, what we assumed indeed corresponds to the terahertz regime in reasonably clean samples of known nodal materials; we discuss below how the scattering time τ can be estimated. Since experimental data on τ is rare, especially for nodal materials which are relatively novel, we shall content ourselves with the following estimation approach. First, consider a representative single NL (e.g., Ca_3P_2 [79]). For a small loop radius, one can work with a continuum model and hence in toroidal coordinates. Consider Coulomb impurities as the dominant scatterers, and take the scatterer concentration to be $\sim 10^{24}\,\mathrm{m}^{-3}$, i.e., of the same order as that of Weyl semimetals such as Cd_3As_2 [80]. For screening, we take the long-wavelength limit to obtain a Thomas-Fermi dielectric function $\varepsilon(\boldsymbol{q}) = 1 + \frac{q_s^2}{\boldsymbol{q}^2}$, where $q_s^2 = e^2\nu(E_F)/\varepsilon_0$ is the square of the inverse screening length, with ν the density of states, ε_0 the vacuum permittivity, and e the elementary charge. To obtain a rough estimate for the relaxation time, one can proceed by assuming that the relaxation time depends only on the Fermi energy. Denoting it as $\tau_{\boldsymbol{k}}$, it can can then be calculated [81] numerically by solving

$$1 = \int \frac{d^3\boldsymbol{k}'}{(2\pi)^3}\frac{2\pi}{\hbar}|\langle\boldsymbol{k}'|\hat{V}|\boldsymbol{k}\rangle|^2\delta(\varepsilon_{\boldsymbol{k}} - \varepsilon_{\boldsymbol{k}'})\left(\tau_{\boldsymbol{k}}^{(i)} - \frac{v_{\boldsymbol{k}'}^{(i)}}{v_{\boldsymbol{k}}^{(i)}}\tau_{\boldsymbol{k}'}^{(i)}\right) \tag{A1}$$

for anisotropic band dispersion $\varepsilon_{\boldsymbol{k}}$. In the above, $\hat{V}$ is the screened impurity potential, and the superscript (i) indicates the direction of the applied field. The resulting relaxation time depends on the Fermi energy, but its values can be placed within the range $\tau \sim 5 \times 10^{-13}\,s$, which is similar to that of graphene as obtained via rf admittance measurements [82]. Then, with a terahertz driving field of frequency $\sim$100 THz,

one has, roughly, $\Omega\tau \sim 50$, validating the ballistic approximation.

APPENDIX B: PROOF OF THE NONMONOTONICITY OF THE RESPONSE OF A TOPOLOGICAL LINKAGE

To show that singularities of the $\mathbf{v} = \nabla_{\mathbf{k}}\varepsilon$ vector field can indeed ensure significant nonlinearity in the current response $\mathbf{J}(\mathbf{A})$, we approximate the Fermi-Dirac distribution $F(\varepsilon)$ as a step function [83] and rewrite the velocity current contribution in a chosen $\hat{e}$ direction as

$$\begin{aligned} J_{\hat{e}}(\mathbf{A}) &= \int F(\varepsilon(\mathbf{k}-\mathbf{A}))\frac{\partial\varepsilon(\mathbf{k})}{\partial k_\parallel}d^3\mathbf{k} \\ &\approx \int \theta(\mu-\varepsilon(\mathbf{k}))\left(\frac{\partial\varepsilon(\mathbf{k}+\mathbf{A})}{\partial k_\parallel}dk_\parallel\right)d\mathbf{k}_\perp \\ &= \int \sum_\alpha \left[\varepsilon\left(\mathbf{k}^\alpha+\Delta\mathbf{k}_\parallel^\alpha+\mathbf{A}\right)-\varepsilon\left(\mathbf{k}^\alpha-\Delta\mathbf{k}_\parallel^\alpha+\mathbf{A}\right)\right]d\mathbf{k}_\perp \\ &= \int \sum_{\alpha\in\text{nodes}} \Delta\varepsilon_\alpha(\mathbf{k}_\perp^\alpha+\mathbf{A})d\mathbf{k}_\perp, \end{aligned} \tag{B1}$$

where $k_\parallel = \mathbf{k}_\parallel\cdot\hat{e} = \mathbf{k}\cdot\hat{e}$ and $\mathbf{k}_\perp = \mathbf{k}-\mathbf{k}_\parallel$ are the components of $\mathbf{k}$ parallel and perpendicular to $\hat{e}$. The BZ is sliced into strips parallel to $\hat{e}$ and indexed by $\mathbf{k}_\perp$, such that the thin nodal Fermi tube is mathematically broken into thin cross sections α in each $\mathbf{k}_\perp$ strip. Each α has a width of $2|\Delta\mathbf{k}_\parallel^\alpha|$ that is determined via $\varepsilon(\mathbf{k}^\alpha\pm\Delta\mathbf{k}_\parallel^\alpha)=\mu$, where $\mathbf{k}^\alpha$ is the central position of α. The current is thus proportional to the sum of all energy differences $\Delta\varepsilon_\alpha(\mathbf{k}_\perp^\alpha) = \varepsilon(\mathbf{k}^\alpha+\Delta\mathbf{k}_\parallel^\alpha+\mathbf{A}) - \varepsilon(\mathbf{k}^\alpha-\Delta\mathbf{k}_\parallel^\alpha+\mathbf{A})$ between the two "sides" of the Fermi tube. This rewriting of current response as shifted boundary terms actually remains valid in arbitrarily high dimensions [84] and can be elegantly expressed in terms of generalized Bianchi identities [85].

Nonlinear response in $J_{\hat{e}}$ can be investigated through the gradient

$$\begin{aligned} &\frac{dJ_{\hat{e}}}{dA_{\hat{e}}} \\ &= \sum_\alpha \frac{d}{dk_\parallel^\alpha}\int\left[\varepsilon\left(\mathbf{k}^\alpha+\Delta\mathbf{k}_\parallel^\alpha+\mathbf{A}\right)-\varepsilon\left(\mathbf{k}^\alpha-\Delta\mathbf{k}_\parallel^\alpha+\mathbf{A}\right)\right]d\mathbf{k}_\perp \\ &\approx 2\int\sum_\alpha \Delta k_\parallel^\alpha\frac{d^2\varepsilon(\mathbf{k}_\perp^\alpha+\mathbf{A})}{dk_\parallel^2}d\mathbf{k}_\perp \\ &= 2\int\sum_\alpha \frac{\mu}{\hat{e}\cdot\mathbf{v}_F}\frac{d^2\varepsilon(\mathbf{k}_\perp^\alpha+\mathbf{A})}{dk_\parallel^2}d\mathbf{k}_\perp, \end{aligned} \tag{B2}$$

where $\hat{e}\cdot\mathbf{v}_F$ is the component of the Fermi velocity of NL α along the applied field. The nonlinear response of the Hopf NL system is guaranteed by its curvature profile (Fig. 7). More generically, the response tensor can be obtained by replacing the second derivative by the Hessian and projecting the Fermi velocity along the applied field. To summarize, Eq. (B2) expresses the current response gradient as the sum of the dispersion curvature over all occupied states, inversely weighted by the Fermi velocity.

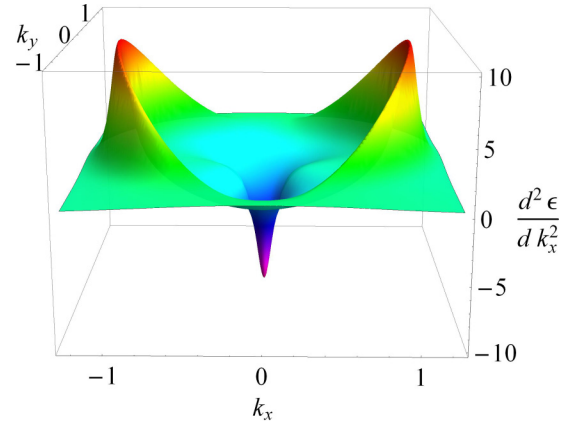

FIG. 7. Plot of the curvature $\frac{d^2\varepsilon}{dk_x^2}$ for the Hopf NL system [Eq. (12)] in the plane of one of its loops, where $k_z = 0$. There are peaks of height $\sim\frac{1}{m_r}$ around the "ears" surrounding the (unit) nodal circumference of the loop, and a sharp trench of depth $\sim\frac{1}{m_0}$ arising from the other perpendicularly impinging loop.

APPENDIX C: ALTERNATIVE MODEL FOR THE SINGLE NODAL LOOP

In the main text, we have mentioned that a single NL has a response nonlinearity that is "unprotected." This is because its dispersion $\varepsilon(\mathbf{k})$ can be deformed, without affecting its ring of nodes, such that its velocity vector field $\mathbf{v} = \nabla_{\mathbf{k}}\varepsilon$ exhibits very different cancellation extents. To illustrate this, we introduce an alternative toy model for the single NL:

$$\begin{aligned} H_{\text{alt}} &= \sin k_x\sigma_x\otimes 1 + \sin k_y\sigma_y\otimes\sigma_y + \sin k_z\sigma_z\otimes 1 + b\sigma_x\otimes\sigma_x \\ &= \begin{bmatrix} \sin k_z & 0 & \sin k_x & b-\sin k_y \\ 0 & \sin k_z & b+\sin k_y & \sin k_x \\ \sin k_x & b+\sin k_y & -\sin k_z & 0 \\ b-\sin k_y & \sin k_x & 0 & -\sin k_z \end{bmatrix}, \end{aligned} \tag{C1}$$

where $0 < b < 1$. This four-band model possesses energy bands

$$\varepsilon_{1,2} = \pm\sqrt{\sin^2 k_z + (\sqrt{\sin^2 k_x+\sin^2 k_y}-b)^2}, \tag{C2}$$

$$\varepsilon_{3,4} = \pm\sqrt{\sin^2 k_z + (\sqrt{\sin^2 k_x+\sin^2 k_y}+b)^2}. \tag{C3}$$

The intersection of the bands $\varepsilon_{1,2}$ of Eq. (C2) forms a single NL in the k_x-k_y plane. But due do their proximity with bands $\varepsilon_{3,4}$, band intersections also exist at the origin, imitating the effect of another node at the center of the NL in the k_x-k_y plane despite the absence of another linked NL. A comparison with the dispersion of the two-band single NL model is shown in Fig. 8. That said, the $\mathbf{v}$ singularity at the center can be easily deformed away from the plane of the NL, thereby reducing the nonlinear response, unlike in the Hopf NL where the central singularity is an unavoidable feature of the nodal linkage.

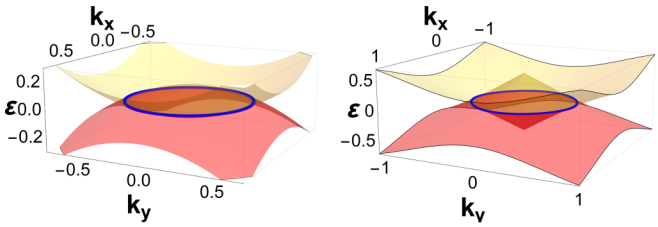

FIG. 8. Conduction (blue) and valence (yellow) bands intersect at a single NL (red) in the (a) two-band single NL model from the main text and (b) the $\varepsilon_{1,2}$ subspace of of the four-band single NL model introduced above. The four-band model contains a divergent curvature at the center of the ring, which gives rise to enhanced though unprotected HHG.

APPENDIX D: FURTHER DETAILS ON THE NODAL MATERIALS AND THEIR LATTICE MODELS

1. Ti_3Al

The energy dispersion of Ti_3Al is modeled by the expression [57]

$$\varepsilon_{\mathrm{Ti_3Al}}(\mathbf{k}) = \frac{1}{2}\left(h_1 + h_2 + \sqrt{(h_1 - h_2)^2 + h^2}\right), \qquad \text{(D1)}$$

where $h_i = A_i(k_x^2 + k_y^2) + B_i k_z^2 + M_i$ and $h = 2Ck_z$ with parameter values $A_1 = -9.66\,\mathrm{eV\,\AA^2}$, $A_2 = 11.37\,\mathrm{eV\,\AA^2}$, $B_1 = 36.22\,\mathrm{eV\,\AA^2}$, $B_2 = -25.71\,\mathrm{eV\,\AA^2}$, $M_1 = 0.12\,\mathrm{eV}$, $M_2 = -0.52\,\mathrm{eV}$, and $C = 22.34\,\mathrm{eV\,\AA^2}$.

To conveniently represent its cross section in the $k_z = 0$ plane, it is also useful to use its piecewise polynomial approximation,

$$\begin{aligned}\varepsilon_{\mathrm{Ti_3Al}}|_{\sqrt{k}\leqslant 0.16} &\approx c_1 + c_2 k,\\ \varepsilon_{\mathrm{Ti_3Al}}|_{\sqrt{k}>0.16} &\approx c_3 + c_4 k + c_5 k^2 + c_6 k^3 + c_7 k^4, \qquad \text{(D2)}\end{aligned}$$

where $k = k_x^2 + k_y^2$ and $c_1 = 0.0911$, $c_2 = -4.0615$, $c_3 = -0.2339$, $c_4 = 9.715$, $c_5 = -41.8543$ $c_6 = 81.1788$ and $c_7 = -59.1387$. Units of energy and momentum k are in eV and $\mathrm{\AA}^{-1}$, respectively. This approximation is a good fit to the dispersion (Fig. 9)

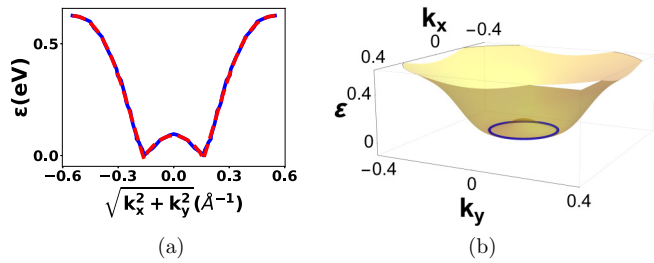

FIG. 9. (a) Comparison of actual dispersion data of Ti_3Al (blue and the best fit piecewise curve (red dashed) along the radial direction in momementum space, i.e., $k = \sqrt{k_x^2 + k_y^2}$; (b) A distinct NL lies at the intersection of the $\pm\varepsilon_{\mathrm{Ti_3Al}}(k_x, k_y, 0)$ bands, i.e., at $\varepsilon(k_x, k_y, 0) = 0$.

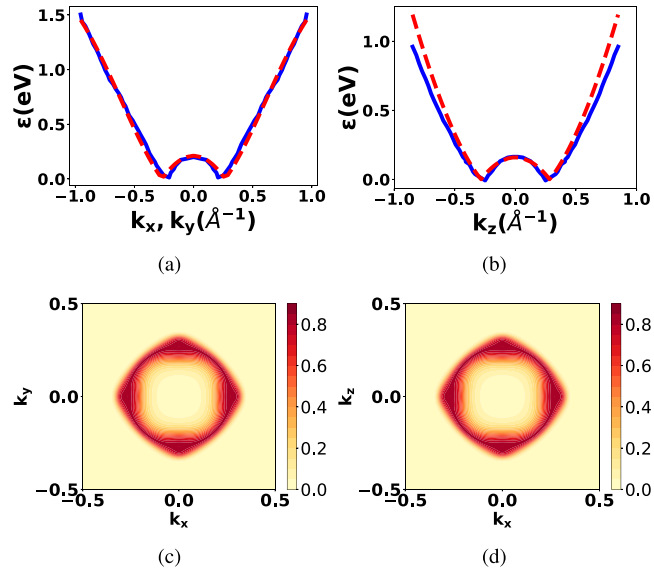

FIG. 10. (a), (b) Comparison of actual dispersion data of YH_3 (blue) and the best fit curve (red dashed) along (a) either the k_x or k_y direction, and (b) the k_z direction; (c), (d) Fermi regions of the YH_3 with $\mu = 0.015eV$ and $T = 10$K along (c) the k_x-k_y plane and (d) the k_x-k_z plane. The color bar indicates the Fermi occupancy factor.

2. YH_3

YH_3 consists of three intersecting NLs along each orthogonal plane in the 3D BZ and can be modeled by the dispersion

$$\varepsilon_{\mathrm{YH_3}}(\mathbf{k}) = \sqrt{\left(g_1^2 + h_1^2\right)\left(g_2^2 + h_2^2\right)\left(g_3^2 + h_3^2\right)}, \qquad \text{(D3)}$$

where the factors $g_i^2 + h_i^2$ each yield an individual NL [86]. They are given by

$$g_1 = \sin(k_z),\ g_2 = \sin(k_x),\ g_3 = \sin(k_y),$$

$$h_1 = a_1(r_1(\cos^3 k_x) + s_1 \cos^3 k_y + t_1 \cos^3 k_z - m_1),$$

$$h_2 = a_2(\cos k_x + \cos k_y + \cos k_z - m_2),$$

$$h_3 = a_3(\cos k_x + \cos k_y + \cos k_z - m_3),$$

where DFT-fitted parameters [61] are given by $m_1 = 2.99$, $a_1 = 2$, $r_1 = s_1 = t_1 = 1.032$, $n_1 = 3$, $m_{2,3} = 2.96$, and $a_{2,3} = 4$. Units of energy and momentum k are eV and $\mathrm{\AA}^{-1}$, respectively. This ansatz is sufficient in taking into account the slight anisotropy in the NLs (Fig. 10).

3. Co_2MnGa

a Tight-binding model

We take the tight-binding model of Co_2MnGa from Ref. [64], which we copy here for ease of reading. It consists of six bands: three d orbitals from Mn and three p orbitals from Ga. In reciprocal space with the basis

$(d_{xz}, d_{yz}, d_{xy}, p_x, p_y, p_z)$, it is given by

$$H(\boldsymbol{k}) = \begin{pmatrix} \xi_1^d & 0 & 0 & \xi_{11}^{dp} & 0 & \xi_{13}^{dp} \\ 0 & \xi_2^d & 0 & 0 & \xi_{22}^{dp} & \xi_{23}^{dp} \\ 0 & 0 & \xi_3^d & \xi_{31}^{dp} & \xi_{32}^{dp} & 0 \\ \xi_{11}^{dp} & 0 & \xi_{31}^{dp} & \xi_1^p & \xi_{12}^p & \xi_{31}^p \\ 0 & \xi_{22}^{dp} & \xi_{32}^{dp} & \xi_{12}^p & \xi_2^p & \xi_{23}^p \\ \xi_{13}^{dp} & \xi_{23}^{dp} & 0 & \xi_{31}^p & \xi_{23}^p & \xi_3^p \end{pmatrix}(\boldsymbol{k}), \quad \text{(D4)}$$

with

$$\xi_1^d(\boldsymbol{k}) = 4t_1 \cos\frac{k_x}{2}\cos\frac{k_z}{2} + 2t_2(\cos k_x + \cos k_z) + 2t_3 \cos k_y + \varepsilon_d, \quad \text{(D5a)}$$

$$\xi_2^d(\boldsymbol{k}) = 4t_1 \cos\frac{k_y}{2}\cos\frac{k_z}{2} + 2t_2(\cos k_y + \cos k_z) + 2t_3 \cos k_x + \varepsilon_d, \quad \text{(D5b)}$$

$$\xi_3^d(\boldsymbol{k}) = 4t_1 \cos\frac{k_x}{2}\cos\frac{k_y}{2} + 2t_2(\cos k_x + \cos k_y) + 2t_3 \cos k_z + \varepsilon_d, \quad \text{(D5c)}$$

$$\xi_1^p(\boldsymbol{k}) = 4t_4 \cos\frac{k_y}{2}\cos\frac{k_z}{2} + 2t_5(\cos k_y + \cos k_z) + 2t_6 \cos k_x + \varepsilon_p, \quad \text{(D5d)}$$

$$\xi_2^p(\boldsymbol{k}) = 4t_4 \cos\frac{k_x}{2}\cos\frac{k_z}{2} + 2t_5(\cos k_x + \cos k_z) + 2t_6 \cos k_y + \varepsilon_p, \quad \text{(D5e)}$$

$$\xi_3^p(\boldsymbol{k}) = 4t_4 \cos\frac{k_x}{2}\cos\frac{k_y}{2} + 2t_5(\cos k_x + \cos k_y) + 2t_6 \cos k_z + \varepsilon_p, \quad \text{(D5f)}$$

$$\xi_{12}^p(\boldsymbol{k}) = -4t_7 \sin\frac{k_x}{2}\sin\frac{k_y}{2}, \quad \text{(D5g)}$$

$$\xi_{23}^p(\boldsymbol{k}) = -4t_7 \sin\frac{k_y}{2}\sin\frac{k_z}{2}, \quad \text{(D5h)}$$

$$\xi_{31}^p(\boldsymbol{k}) = -4t_7 \sin\frac{k_x}{2}\sin\frac{k_z}{2}, \quad \text{(D5i)}$$

$$\xi_{11}^{dp}(\boldsymbol{k}) = \xi_{22}^{dp}(\boldsymbol{k}) = 2t_8 \sin\frac{k_z}{2}, \quad \text{(D5j)}$$

$$\xi_{13}^{dp}(\boldsymbol{k}) = \xi_{32}^{dp}(\boldsymbol{k}) = 2t_8 \sin\frac{k_x}{2}, \quad \text{(D5k)}$$

$$\xi_{23}^{dp}(\boldsymbol{k}) = \xi_{31}^{dp}(\boldsymbol{k}) = 2t_8 \sin\frac{k_y}{2}, \quad \text{(D5l)}$$

where the fitted tight-binding parameters are given (in units of eV) by $t_1 = -0.31, t_2 = -0.018, t_3 = -0.01, t_4 = 0.2, t_5 = -0.02, t_6 = 0.04, t_7 = 0.28, t_8 = -0.34, \varepsilon_d = -0.6, \varepsilon_p = 0.6$.

b Velocity field in the nodal Co_2MnGa network

The velocity field of Co_2MnGa as illustrated in Fig. 11 is the basis of detailed analysis of the shape of its response current. We consider the current contribution of the green and yellow nodal structures in the top panel of Fig. 5(a) of the main text. In Fig. 5(b)(A), we mark several points for the drift p_0, and study the resulting drifted Fermi surface, as well as the change of the velocity occupied by it. The sharp increase

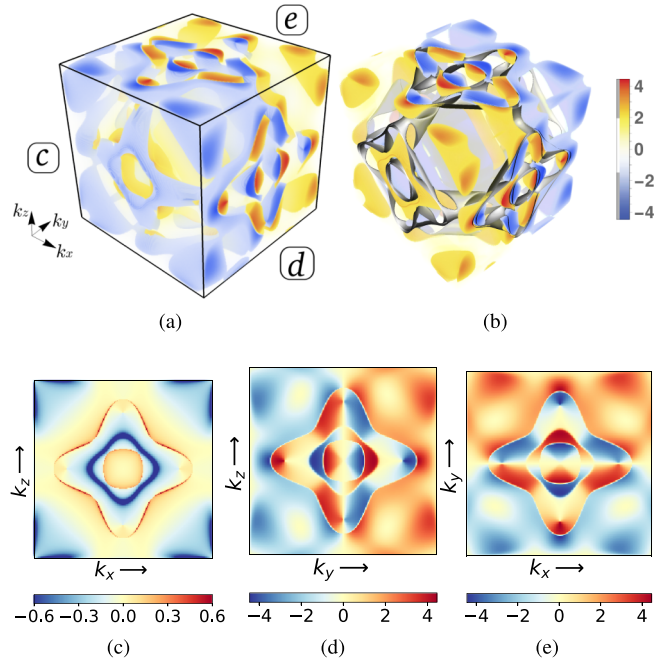

FIG. 11. (a) The density plot of v_y, i.e., the y component of the group velocity of the third band (ordered from high to low energies) of the tight-binding model of Co_2MnGa. The choice of the velocity component is arbitrary owing to the cubic symmetry of Co_2MnGa. The planes labeled (c)–(e) correspond to the cross sections on which we display v_y below. (b) A rotated view of (a), overlaid by the Fermi surface of Co_2MnGa. (c) Density plot of v_y restricted on the k_z-k_x plane at $k_y = -2\pi/a$. (d) Density plot of v_y on the k_z-k_y plane at $k_x = 2\pi/a$. (e) Density plot of v_y on the k_y-k_x plane at $k_z = 2\pi/a$. All color bars are expressed in units of $\times 10^5$ ms^{-1}.

from (i) to (ii) is a consequence of the rapidly varying velocity field, as soon as the Fermi surface is driven even slightly away from equilibrium. This sharp increase soon saturates and begins to fall as the flower petal is shifted away from the intense red patches situated near the touching points of the inner and outer chains [(ii) to (iv)]. Going from (iv) to (v), the current eventually changes signs because the intense blue patches are now being sampled, The current slowly becomes positive again [(v) to (vi)] when the flower petal is shifted to the outer chain [Fig. 6(b)].

In contrast to the current due to the green nodal structure [Fig. 5(b)(A)], the gradient of the current is not as steep for the yellow structure [Fig. 5(c)(A)]. Furthermore, the yellow circular ring also contributes exclusively negative velocity [Fig. 5(c)(i–vi)] within the drift considered here, unlike the green one where the regions occupied by the ring vary in sign [Fig. 5(b)(i)–(vi)]. These observations, together with the evolution of the velocity field similar to that discussed in the previous paragraph, can account for the current pattern of the yellow nodal structure.

The above analysis demonstrates how the strong inhomogeneity of the velocity field, which results from the knotted links and touching loops, gives rise to its characteristic response. Indeed, on the two high symmetry planes displayed in Figs. 11(d) and 11(e), the flower petals are clearly discernible as contours of sign-changing points. As shown in Fig. 11(b), the Fermi surface of Co_2MnGa fits matchingly the void of

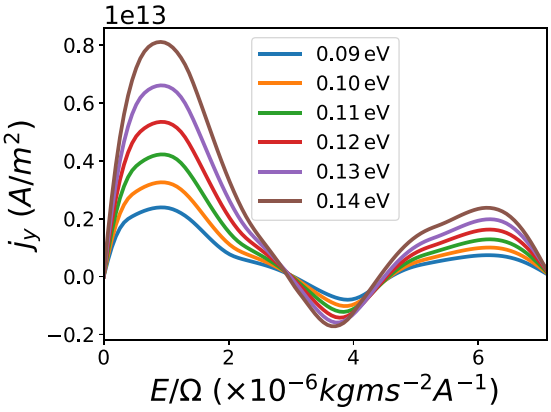

FIG. 12. Response current of Co_2MnGa for different values of chemical potential μ. A qualitatively similar curve persists, even though larger chemical potentials (thicker nodal regions) give rise to larger currents in general.

the velocity field. By visualizing the velocity fields of simpler artificial nodal links (not shown), we observe that the more complicated a nodal network, the more often the velocity field switches direction. Our analysis holds best for small chemical potentials that result in thin NLs, even though the response curve usually remains qualitatively preserved as the chemical potential is increased (Fig. 12), unless the NLs become so thick that they fuse and generate different nodal topologies.

4. Individual plots of the Fourier harmonics from HHG

In Fig. 13, we present more detailed data of the individual higher harmonics generated from our selected nodal materials in increasing level of complexity.

5. Comments on our theoretical approach

Here we comment on our approach and connect it to a few experimental breakthroughs on HHG in solids. Throughout this paper, we compute the electrical current by solving the semiclassical EOMs to obtain the electronic velocity, which is then integrated over the phase space, weighted by the distribution function dictated by the Boltzmann equation.

From explaining the Wiedemann-Franz law to predicting the Bloch oscillation, such an approach has been hugely successful since the dawn of the quantum theory of solids [87]. The semiclassical EOMs with "anomalous velocity" corrections are not only conceptually appealing but also predictively powerful in explaining diverse phenomena such as the various Hall effects and quantum oscillations [42]. As for the Boltzmann equation, it is expected to work best for weakly interacting systems which can be well described by the Landau theory of Fermi liquid [47]. While the importance of correlation effects in nodal systems is certainly material dependent, the fact that DFT+ARPES calculations of Co_2MnGa match so nicely the experimental results [88] may hint that a tight-binding description of quasiparticles, and hence the application of the Boltzmann equation, should be a good starting point.

In general, solving the Boltzmann equation is highly nontrivial, complicated by the collision integral that assumes different forms and requires various approximation schemes, depending on the scattering mechanisms. Confronted with this difficulty, progress can be made by working within the RTA, where the collision integral is assumed to take the form $(F - f)/\tau$. This approximation is motivated by the consideration that various types of scattering (electron-phonon, electron-impurity, electron-electron) will relax the system to a distribution F (often chosen to be the Fermi-Dirac distribution) within a timescale τ which can be computed if a microscopic model for the scattering processes is given [48].

In our paper, the collision integral is completely neglected. One way to justify this is as follows. Invoking the constant RTA, one has $(\partial_t + \dot{\boldsymbol{p}}(t) \cdot \partial_{\boldsymbol{p}}) f = (F - f)/\tau$, where f is the distribution function, $\boldsymbol{p}$ the momentum. In the presence of a periodic electric field of frequency Ω [which enters the equation via $\dot{\boldsymbol{p}}(t)$], it is reasonable to assume a periodic steady state, provided the driving force is not too weak and not too slow compared to the dissipative relaxing term. Then, a periodic average of the equation implies that the left-hand side is of the order $O(\Omega\tau)$, and the right-hand side of order $O(1)$, so for $\Omega\tau \gg 1$, the collision term may be ignored altogether. This conforms to the intuition that scattering is not so relevant in presence of a fast driving field [44].

As with most physical sciences, theoretical descriptions of HHG in solids admit a varying degree of sophistication. For example, one may wish to examine the spatial distribution of the harmonics by taking a Wannier representation for the

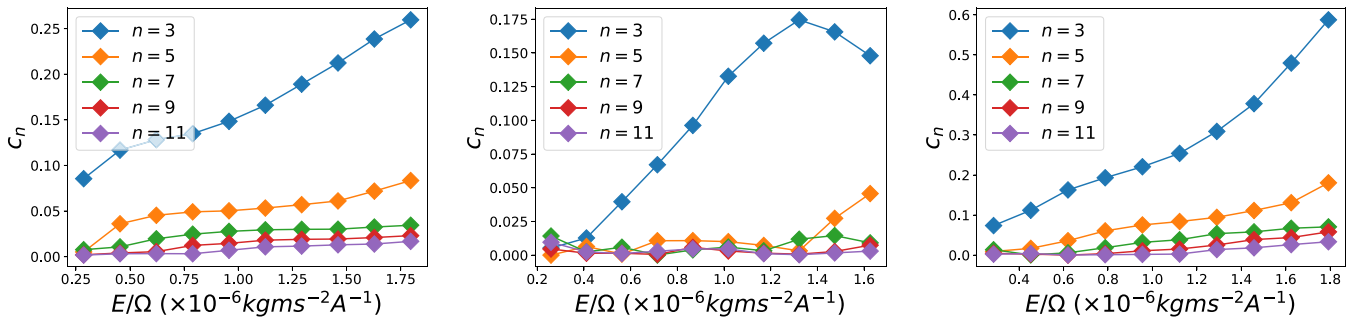

(a) Ti_3Al (b) YH_3 (c) Co_2MnGa

FIG. 13. Higher harmonic generation (normalized by the first harmonic) for different field strengths p_0 in (a) single nodal loop Ti_3Al, (b) triple inner chain YH_3, (c) nodal network Co_2MnGa. Note that the harmonic amplitudes c_n for different materials are plotted in different scales across these figures; they are compared side by side in the same figure [Fig. 4(e)] in the main text.

valence bands [89], or to study the contributions of interband current by adding an interband polarization term [90], or to account for the Coulomb interaction via a dephasing term [91]. For the purpose of illustrating the HHG due to topologically enforced nonlinearities in linked NLSMs, we considered only the intraband current within a noninteracting picture. This approach closely mirrors the theoretical model developed in the groundbreaking observation of HHG in bulk ZnO [92]. There, a Peierl's substitution of a continuous wave electric field is performed on a single band of ZnO. The current is computed by multiplying the velocity with the electron charge and density. Simply by taking into account longer-range hoppings, qualitative features including the linear energy cutoff of the experimental HHG can already be captured. In our current expression, $J[\mathbf{A}(t)] = e\int_{\mathrm{BZ}} \frac{d^3\boldsymbol{p}}{(2\pi\hbar)^3} f[\varepsilon(\boldsymbol{p}-\boldsymbol{p}(t))]\boldsymbol{v}(\boldsymbol{p})$, upon a coordination transformation, the electric field $\boldsymbol{p}(t)$ dependence turns up in the velocity, and the expression becomes similar to that in Ref. [92], with the exception that we integrate over the BZ instead of evaluating it at a certain momentum. We note that similar semiclassical approaches have subsequently been employed in Ref. [43] to discuss Bloch oscillations in HHG, as well as in Ref. [44] to study the role of Berry curvature in HHG of monolayer MoS_2. With regard to scattering and many-body effects, rather reassuringly, they should play only minor roles in HHG experiments [44,49], in accordance with the intuition that most scattering cannot keep up with the fast driving field. Together with the fact that interactions are mostly insignificant in symmetry-protected topological materials, our theoretical approach may prove sufficient to describe HHG in nodal-line semimetals.

[1] M. König, S. Wiedmann, C. Brüne, A. Roth, H. Buhmann, L. W. Molenkamp, X.-L. Qi, and S.-C. Zhang, Science **318**, 766 (2007).

[2] A. Marrazzo, M. Gibertini, D. Campi, N. Mounet, and N. Marzari, Phys. Rev. Lett. **120**, 117701 (2018).

[3] Z. Liu, G. Zhao, B. Liu, Z. F. Wang, J. Yang, and F. Liu, Phys. Rev. Lett. **121**, 246401 (2018).

[4] A. R. Mellnik, J. S. Lee, A Richardella, J. L. Grab, P. J. Mintun, M. H. Fischer, A. Vaezi, A. Manchon, E.-A. Kim, N. Samarth *et al.*, Nature **511**, 449 (2014).

[5] S. Zhang and X. Zhang, U.S. Patent No. 9,024,415, May 5 2015.

[6] S. Zhang and J. Wang, U.S. Patent App. No. 14/447,499, Feb 4 2016.

[7] S. Zhang and J. Wang, U.S. Patent No. 9,362,227, Jun 7 2016.

[8] W. Wu, Y. Liu, S. Li, C. Zhong, Z.-M. Yu, X.-L. Sheng, Y. X. Zhao, and S. A. Yang, Phys. Rev. B **97**, 115125 (2018).

[9] C. Fang, Y. Chen, H.-Y. Kee, and L. Fu, Phys. Rev. B **92**, 081201(R) (2015).

[10] W. Chen, H.-Z. Lu, and J.-M. Hou, Phys. Rev. B **96**, 041102(R) (2017).

[11] Z. Yan, R. Bi, H. Shen, L. Lu, S.-C. Zhang, and Z. Wang, Phys. Rev. B **96**, 041103(R) (2017).

[12] J. Ahn, D. Kim, Y. Kim, and B.-J. Yang, Phys. Rev. Lett. **121**, 106403 (2018).

[13] G. Bian, T.-R. Chang, R. Sankar, S.-Y. Xu, H. Zheng, T. Neupert, C.-K. Chiu, S.-M. Huang, G. Chang, I. Belopolski *et al.*, Nat. Commun. **7**, 10556 (2016).

[14] A. Crepaldi, L. A. G. T. Moreschini, G. Autes, C. Tournier-Colletta, S. Moser, N. Virk, H. Berger, Ph. Bugnon, Y. J. Chang, K. Kern *et al.*, Phys. Rev. Lett. **109**, 096803 (2012).

[15] J. Hu, Z. Tang, J. Liu, X. Liu, Y. Zhu, D. Graf, K. Myhro, S. Tran, C. N. Lau, J. Wei *et al.*, Phys. Rev. Lett. **117**, 016602 (2016).

[16] D.-Y. Chen, Y. Wu, L. Jin, Y. Li, X. Wang, J. Duan, J. Han, X. Li, Y.-Z. Long, X. Zhang, D. Chen, and B. Teng, Phys. Rev. B **100**, 064516 (2019).

[17] C.-J. Yi, B. Q. Lv, Q. S. Wu, B.-B. Fu, X. Gao, M. Yang, X.-L. Peng, M. Li, Y.-B. Huang, P. Richard *et al.*, Phys. Rev. B **97**, 201107(R) (2018).

[18] X.-L. Qi, T. L. Hughes, and S.-C. Zhang, Phys. Rev. B **78**, 195424 (2008).

[19] A. P. Schnyder, S. Ryu, A. Furusaki, and A. W. W. Ludwig, Phys. Rev. B **78**, 195125 (2008).

[20] L. Li, C. H. Lee, and J. Gong, Phys. Rev. Lett. **121**, 036401 (2018).

[21] M. R. Dennis, R. P. King, B. Jack, K. O'Holleran, and M. J. Padgett, Nat. Phys. **6**, 118 (2010).

[22] C. H. Lee, G. Li, Y. Liu, T. Tai, R. Thomale, and X. Zhang, arXiv:1812.02011.

[23] I. Belopolski, D. S. Sanchez, G. Chang, K. Manna, B. Ernst, S.-Y. Xu, S. S. Zhang, H. Zheng, J. Yin, B. Singh, G. Bian, D. Multer, X. Zhou, S.-M. Huang, B. Wang, A. Bansil, H. Lin, C. Felser, and M. Zahid Hasan, arXiv:1712.09992.

[24] L. Tráng and C. P. Ramanujam, Am. J. Math. **98**, 67 (1976).

[25] K. Murasugi, *Knot Theory and its Applications* (Springer Science & Business Media, New York, 2007).

[26] M. Stålhammar, L. Rødland, G. Arone, J. C. Budich, and E. J. Bergholtz, SciPost Phys. **7**, 019 (2019).

[27] More precisely, the topological class of the Fermi region configuration around the nodal loops.

[28] W. Chen, H.-Z. Lu, and O. Zilberberg, Phys. Rev. Lett. **122**, 196603 (2019).

[29] W. Chen, K. Luo, L. Li, and O. Zilberberg, Phys. Rev. Lett. **121**, 166802 (2018).

[30] T. Li, L. Duca, M. Reitter, F. Grusdt, E. Demler, M. Endres, M. Schleier-Smith, I. Bloch, and U. Schneider, Science **352**, 1094 (2016).

[31] N. Fläschner, B. S. Rem, M. Tarnowski, D. Vogel, D.-S. Lühmann, K. Sengstock, and C. Weitenberg, Science **352**, 1091 (2016).

[32] G. Vampa, T. J. Hammond, M. Taucer, X. Ding, X. Ropagnol, T. Ozaki, S. Delprat, M. Chaker, N. Thiré, B. E. Schmidt *et al.*, Nat. Photonics **12**, 465 (2018).

[33] A. Chacón, W. Zhu, S. P. Kelly, A. Dauphin, E. Pisanty, D. Kim, D. E. Kim, A. Picón, C. Ticknor, M. F. Ciappina *et al.*, arXiv:1807.01616.

[34] S. Ghimire and D. A. Reis, Nat. Phys. **15**, 10 (2019).

[35] B. Cheng, N. Kanda, T. N. Ikeda, T. Matsuda, P. Xia, T. Schumann, S. Stemmer, J. Itatani, N. P. Armitage, and R. Matsunaga, Phys. Rev. Lett. **124**, 117402 (2020).

[36] S. Kovalev, R. M. A. Dantas, S. Germanskiy, J.-C. Deinert, B. Green, I. Ilyakov, N. Awari, M. Chen, M. Bawatna, J. Ling *et al.*, Nat. Commun. **11**, 2451 (2020).

[37] Y. Gao, S. Kaushik, E. J. Philip, Z. Li, Y. Qin, Y. P. Liu, W. L. Zhang, Y. L. Su, X. Chen, H. Weng *et al.*, Nat. Commun. **11**, 720 (2020).

[38] T. Morimoto, S. Zhong, J. Orenstein, and J. E. Moore, Phys. Rev. B **94**, 245121 (2016).

[39] A. A. Zyuzin and A. Yu. Zyuzin, Phys. Rev. B **95**, 085127 (2017).

[40] P. Tassin, T. Koschny, and C. M. Soukoulis, Science **341**, 620 (2013).

[41] Y. Sun, M. Y. Sy, Yi-Xiang J Wang, A. T. Ahuja, Y.-T. Zhang, and E. Pickwell-MacPherson, World J. Radiology **3**, 55 (2011).

[42] D. Xiao, M.-C. Chang, and Q. Niu, Rev. Mod. Phys. **82**, 1959 (2010).

[43] O. Schubert, M. Hohenleutner, F. Langer, B. Urbanek, C. Lange, U. Huttner, D. Golde, T. Meier, M. Kira, S. W. Koch *et al.*, Nat. Photonics **8**, 119 (2014).

[44] H. Liu, Y. Li, Y. S. You, S. Ghimire, T. F. Heinz, and D. A. Reis, Nat. Phys. **13**, 262 (2017).

[45] Refer to Appendixes.

[46] Normalization implicit integration measure.

[47] R. Kubo, *The Boltzmann Equation* (Springer, Vienna, 1973), pp. 301–340.

[48] D. Y. H. Ho, I. Yudhistira, N. Chakraborty, and S. Adam, Phys. Rev. B **97**, 121404(R) (2018).

[49] G. Ndabashimiye, S. Ghimire, M. Wu, D. A. Browne, K. J. Schafer, M. B. Gaarde, and D. A. Reis, Nature **534**, 520 (2016).

[50] S. A. Mikhailov, Europhys. Lett. **79**, 27002 (2007).

[51] Incidentally, it also mirrors the theoretical model for a different HHG mechanism observed in bulk ZnO [92].

[52] L. Wu, S. Patankar, T. Morimoto, N. L. Nair, E. Thewalt, A. Little, J. G. Analytis, J. E. Moore, and J. Orenstein, Nat. Phys. **13**, 350 (2017).

[53] H. A. Hafez, S. Kovalev, J.-C. Deinert, Zoltán Mics, B. Green, N. Awari, M. Chen, S. Germanskiy, U. Lehnert, J. Teichert *et al.*, Nature **561**, 507 (2018).

[54] C. H. Lee, X. Zhang, and B. Guan, Sci. Rep. **5**, 18008 (2015).

[55] C. H. Lee, T. Hofmann, T. Helbig, Y. Liu, X. Zhang, M. Greiter, and R. Thomale, arXiv:1904.10183.

[56] Qualitatively, these gaps can represent the smudging of the Fermi tube due to nonzero temperature.

[57] X. Zhang, Z.-M. Yu, Z. Zhu, W. Wu, S.-S. Wang, X.-L. Sheng, and S. A. Yang, Phys. Rev. B **97**, 235150 (2018).

[58] E. A. Basuki, M. I. Yuliansyah, F. M. Rahman, F. Muhammad, and D. Prajitno, J. Eng. Technol. Sci. **48**, 534 (2016).

[59] K. L. Yang, J. C. Huang, and Y. N. Wang, Acta Mater. **51**, 2577 (2003).

[60] S. Chen, Y. Chen, H. Zhang, Y. Tang, J. Wei, and W. Sun, J. Nanomaterials **2013**, 131 (2013).

[61] D. Shao, T. Chen, Q. Gu, Z. Guo, P. Lu, J. Sun, L. Sheng, and D. Xing, Sci. Rep. **8**, 1467 (2018).

[62] V. K. Fedotov, V. E. Antonov, I. O. Bashkin, T. Hansen, and I. Natkaniec, J. Phys.: Condens. Matter **18**, 1593 (2006).

[63] T. J. Udovic, Q. Huang, A. Santoro, and J. J. Rush, Z. für Kristallogr. - Cryst. Mater. **223**, 697 (2008).

[64] G. Chang, S.-Y. Xu, X. Zhou, S.-M. Huang, B. Singh, B. Wang, I. Belopolski, J. Yin, S. Zhang, A. Bansil, H. Lin, and M. Z. Hasan, Phys. Rev. Lett. **119**, 156401 (2017).

[65] S. N. Guin, K. Manna, J. Noky, S. J. Watzman, C. Fu, N. Kumar, W. Schnelle, C. Shekhar, Y. Sun, J. Gooth *et al.*, NPG Asia Mater. **11**, 16 (2019).

[66] A. Markou, D. Kriegner, J. Gayles, L. Zhang, Y.-C. Chen, B. Ernst, Y.-H. Lai, W. Schnelle, Y.-H. Chu, Y. Sun *et al.*, Phys. Rev. B **100**, 054422 (2019).

[67] Not only were various smaller nodal features omitted from the dispersion, the Fermi regions were also restricted to the individual features.

[68] W.-J. Chen, M. Xiao, and C. T. Chan, Nat. Commun. **7**, 13038 (2016).

[69] J. Y. Lin, N. C. Hu, Y. J. Chen, C. H. Lee, and X. Zhang, Phys. Rev. B **96**, 075438 (2017).

[70] W. Gao, B. Yang, B. Tremain, H. Liu, Q. Guo, L. Xia, A. P. Hibbins, and S. Zhang, Nat. Commun. **9**, 1 (2018).

[71] Q. Yan, R. Liu, Z. Yan, B. Liu, H. Chen, Z. Wang, and L. Lu, Nat. Phys. **14**, 461 (2018).

[72] M. Kim, D. Lee, D. Lee, and J. Rho, Phys. Rev. B **99**, 235423 (2019).

[73] X. Zhang, Y. Chen, Y. Wang, Y. Liu, J. Y. Lin, N. C. Hu, B. Guan, and C. H. Lee, Phys. Rev. B **100**, 041110(R) (2019).

[74] L. Xia, Q. Guo, B. Yang, J. Han, C.-X. Liu, W. Zhang, and S. Zhang, Phys. Rev. Lett. **122**, 103903 (2019).

[75] K. Luo, R. Yu, H. Weng *et al.*, Research **2018**, 6793752 (2018).

[76] L. Li, C. H. Lee, and J. Gong, Commun. Phys. **2**, 135 (2019).

[77] However, topolectrical circuits that are intrinsically nonlinear [78] can also exhibit higher harmonic generation.

[78] Y. Wang, L.-J. Lang, C. H. Lee, B. Zhang, and Y. Chong, Nat. Commun. **10**, 1102 (2019).

[79] L. S. Xie, L. M. Schoop, E. M. Seibel, Q. D. Gibson, W. Xie, and R. J. Cava, APL Mater. **3**, 083602 (2015).

[80] N. Ramakrishnan, M. Milletari, and S. Adam, Phys. Rev. B **92**, 245120 (2015).

[81] J. Schliemann and D. Loss, Phys. Rev. B **68**, 165311 (2003).

[82] E. Pallecchi, A. C. Betz, J. Chaste, G. Fève, B. Huard, T. Kontos, J.-M. Berroir, and B. Plaçais, Phys. Rev. B **83**, 125408 (2011).

[83] This introduces negligible errors at room temperature.

[84] C. H. Lee, Y. Wang, Y. Chen, and X. Zhang, Phys. Rev. B **98**, 094434 (2018).

[85] I. Petrides, H. M. Price, and O. Zilberberg, Phys. Rev. B **98**, 125431 (2018).

[86] Y. Zhou, F. Xiong, X. Wan, and J. An, Phys. Rev. B **97**, 155140 (2018).

[87] J. M. Ziman, *Electrons and Phonons: The Theory of Transport Phenomena in Solids* (Oxford University Press, Oxford, UK, 2001).

[88] I. Belopolski, D. S. Sanchez, G. Chang, K. Manna, B. Ernst, S.-Y. Xu, S. S. Zhang, H. Zheng, J. Yin, B. Singh *et al.*, arXiv:1712.09992 .

[89] E. N. Osika, A. Chacón, L. Ortmann, N. Suárez, J. A. Pérez-Hernández, Bartłomiej Szafran, M. F. Ciappina, F. Sols, A. S. Landsman, and M. Lewenstein, Phys. Rev. X **7**, 021017 (2017).

[90] G. Vampa, C. R. McDonald, G. Orlando, P. B. Corkum, and T. Brabec, Phys. Rev. B **91**, 064302 (2015).

[91] D. Golde, T. Meier, and S. W. Koch, JOSA B **23**, 2559 (2006).

[92] S. Ghimire, A. D. DiChiara, E. Sistrunk, P. Agostini, L. F. DiMauro, and D. A. Reis, Nat. Phys. **7**, 138 (2011).